Die Grenzen der Chemie neu ausloten? It takes #HumanChemistry

Wir suchen kreative Chemikerinnen und Chemiker, die mit uns gemeinsam neue Wege gehen wollen – mit Fachwissen, Unternehmertum und Kreativität für innovative Lösungen. Informieren Sie sich unter:

evonik.de/karriere

evonik
Leading Beyond Chemistry

Anisometric Microstructures to Determine Minimal Critical Physical Cues Required for Neurite Alignment

Sitara Vedaraman, Amaury Perez-Tirado, Tamas Haraszti, Jose Gerardo-Nava, Akihiro Nishiguchi, and Laura De Laporte*

In nerve regeneration, scaffolds play an important role in providing an artificial extracellular matrix with architectural, mechanical, and biochemical cues to bridge the site of injury. Directed nerve growth is a crucial aspect of nerve repair, often introduced by engineered scaffolds imparting linear tracks. The influence of physical cues, determined by well-defined architectures, has been mainly studied for implantable scaffolds and is usually limited to continuous guiding features. In this report, the potential of short anisometric microelements in inducing aligned neurite extension, their dimensions, and the role of vertical and horizontal distances between them, is investigated. This provides crucial information to create efficient injectable 3D materials with discontinuous, in situ magnetically oriented microstructures, like the Anisogel. By designing and fabricating periodic, anisometric, discreet guidance cues in a high-throughput 2D in vitro platform using two-photon lithography techniques, the authors are able to decipher the minimal guidance cues required for directed nerve growth along the major axis of the microelements. These features determine whether axons grow unidirectionally or cross paths via the open spaces between the elements, which is vital for the design of injectable Anisogels for enhanced nerve repair.

1. Introduction

Implantable and injectable artificial scaffolds, such as conduits,[1–4] fibers,[5,6] and hydrogels[7] have been developed to promote directed nerve growth after injury. The internal structure of implantable scaffolds generally contains an aligned architecture in the form of long fibers, elongated pores, or channels that provide physical and mechanical guiding stimuli to enable oriented nerve growth.[8] The presence of directional cues inside the biomaterial scaffolds is crucial to facilitate reconnection of the nerves with their appropriate targets[9] to regain partial or complete function. More recently, research has focused on creating injectable materials with the ability to form anisotropic structures.[10] This is important to create low-invasive therapies for soft, oriented neuronal tissues, such as the spinal cord. For example, the Anisogel consists of magneto-responsive rod-shaped microgels or short fibers that orient in situ in the presence of a low magnetic field, while a surrounding hydrogel precursor solution crosslinks to immobilize the 3D anisotropic structure after removal of the magnetic field.[11] Compared to implants, the Anisogel system consists of small injectable alignable elements that lead to discontinuous, individually aligned guiding structures that span the entire length of the material. Therefore, understanding the effect of the structure dimensions and aspect ratios, and the vertical and horizontal distances between the elements is an important step toward successfully steering neurite growth in a linear manner. However, we believe that the currently reported material systems have not yet studied the effect of discrete anisometric topographic elements in a controlled manner.

So far, continuous topographies, such as long patterned lines (ridges and grooves),[12–15] nanowires,[16] and fibers,[17,18]

S. Vedaraman, A. Perez-Tirado, Dr. T. Haraszti, Dr. J. Gerardo-Nava, Prof. L. De Laporte
DWI-Leibniz Institute for Interactive Materials
Forckenbeckstrasse 50, Aachen 52074, Germany
E-mail: delaporte@dwi.rwth-aachen.de

S. Vedaraman, Dr. T. Haraszti, Prof. L. De Laporte
Institute for Technical and Macromolecular Chemistry
RWTH Aachen
Worringerweg 1–2, Aachen 52074, Germany

Dr. A. Nishiguchi
Biomaterials Field
Research Center for Functional Materials
National Institute for Materials Science
Tsukuba 305-0044, Japan

Prof. L. De Laporte
Institute of Applied Medical Engineering
Department of Advanced Materials for Biomedicine
RWTH University
Forckenbeckstraße 55, Aachen 52074, Germany

**ADVANCED
SCIENCE NEWS**

www.advancedsciencenews.com

**ADVANCED
HEALTHCARE
MATERIALS**

www.advhealthmat.de

or discontinuous topographies, such as nano-[19] and micro-pillars[20–22] have been produced to study directed growth of neural or neurogenic cells. Microfabrication technologies, such as etching,[22] electro/dry spinning,[23] soft-lithography,[15] photolithography,[24] and wrinkle formation[25] have been employed to fabricate these nano- and micro-interfaces with a wide range of materials and architectures to gain further information on cell–material interactions.[26,27] For example, topographies that mimic native extra cellular matrix (ECM) were developed by inverse molding of aligned Schwann cells on patterned glass surface. The obtained polydimethylsiloxane (PDMS) films were rolled into conduits with Schwann-cell like topographies oriented parallel to the axis of the conduit, resulting in increased neurite guidance compared to topographies oriented perpendicular to the long axis of the conduit.[28] A study with continuous grooves and ridges with equal widths (periodicity 20 µm) on a PDMS film reported higher Schwann cell alignment with groove depths of 2.5 µm compared to flat or lower lateral groove dimensions (periodicity: 4 or 1 µm) and depths (850 or 350 nm).[15] In another study with continuous microgrooves and ridges (depth 1 µm) developed with photo-lithography of methacrylate polymers, reduced nerve alignment was observed when the lateral distance increased from 10 to 50 µm, while neurite orientation improved for deeper pattern depth up to 8 µm.[29] On a smaller scale, nano ridges with widths ranging between 100 and 800 nm demonstrated preferential nerve growth on the ridges, while the highest alignment was observed on equally spaced ridges and grooves of 200 nm each.[30] Compared to sharp edge patterns, gradually sloping grooves and ridges were produced, demonstrating that the optimal lateral groove spacing for oriented nerve growth was dependent on the groove depth. Maximum alignment of spiral ganglion neurons was achieved on both lateral spacings at 50 or 10 µm at a groove depth of 8 or 1 µm, respectively.[24] Wrinkles with even more natural features created via uniaxial mechanical stretching/plasma treatment of PDMS indicated that the inter-wrinkle distances (width) dominate the effect on cell alignment in comparison to the amplitude (depth) of the wrinkles.[31] A wrinkle width of 26 µm and amplitude of 2.9 µm allowed for differentiation of human bone marrow-derived MSCs to neurons, thus exploring topography-mediated neuronal differentiation.[32]

In contrast to continuous patterns, the role of substrates with discontinuous guiding elements has not been widely explored. Isometric micropillars with dimensions of 1–2 µm and interpillar distances of 1–2 µm were fabricated with ion etching techniques and guided nerve cells in a straight path.[21] Here, the shape of the isometric pillars determines the direction of neurite growth, for example, hexagonal micropillars (width 1.6 µm and height 3 µm), with inter-pillar distances of 1.4 µm reported linear neurite extension in six preferred growth directions following the edges of the hexagonal shape.[33] Therefore, the physical guidance afforded by the micropillars failed to provide one primary growth direction, while continuous guiding cues induced unidirectional growth.[34] In the case of discreet topographies, the ability to retain the growth direction is influenced by the dimensions, aspect ratio, and inter-elemental spacing of the elements. For example, discontinuous elliptical microcones (spikes) with subcellular dimensions, fabricated by laser irradiation on Si wafer and oriented parallel to one another show improved neurite alignment.[35] Despite their ability to direct neurite growth, a lack of control in
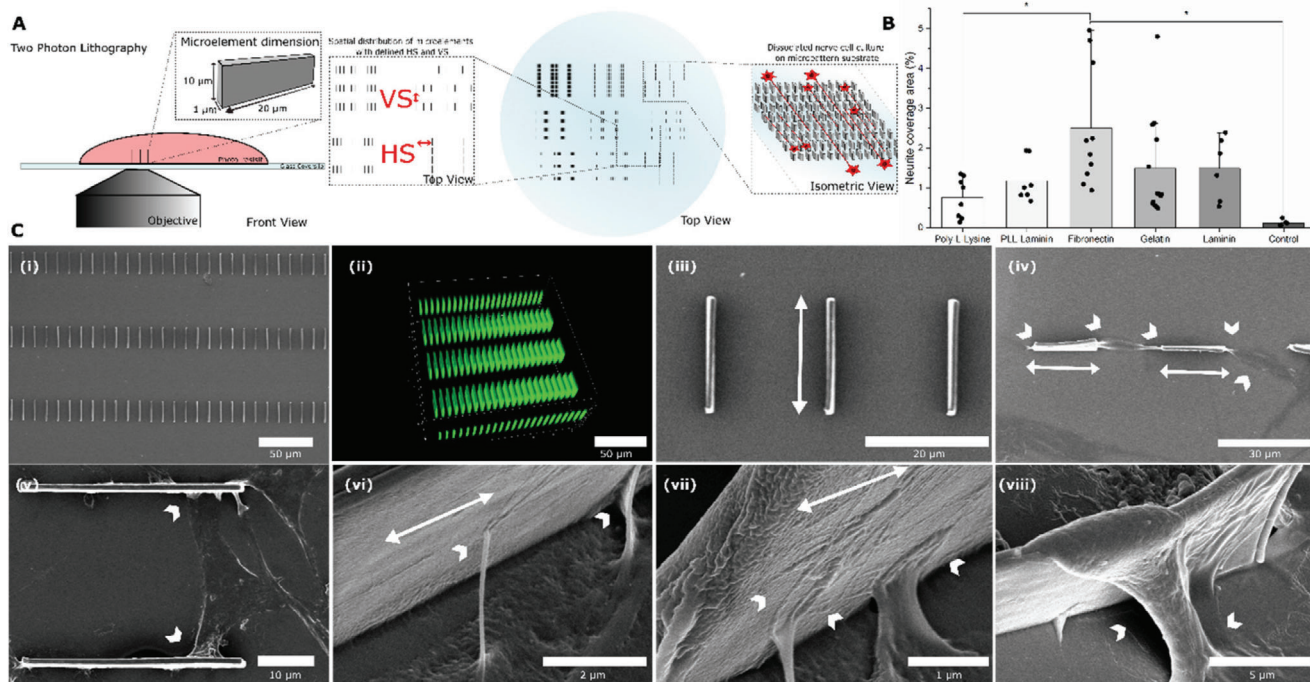
the spatial positioning and architecture of microcones using this technique limits its applicability as a screening technology for our purpose. In another study, discreet anisometric rectangular (length: 45 µm, width: 3 µm) nano-high ridges were fabricated via photolithography at fixed inter-element distances (vertical spacing: 6 µm, horizontal spacing: 30 µm), demonstrating that for low topographies between 10 and 50 nm, the alignment of the neurites with the nanoridges depends on the angle of incidence, while for higher nanoridges above 50 nm, growth cones reaching the elements in a perpendicular manner will still move parallel to the ridges.[36,37]

Despite much progress in the field, a good understanding of the effect of dimensions and aspect ratio of discrete elements, and the vertical and horizontal distances between them, on unidirectional nerve growth, is still unknown, but an important step to develop injectable materials that form anisotropic structures in situ, such as the Anisogel.[10] These materials are extremely important for creating low-invasive therapies to repair and regenerate soft, oriented tissues, such as the spinal cord. To study this without the inherent variability of the distances between anisometric microstructures inside the 3D constructs after injection, we present a simplified platform using two-photon lithography (TPL) technique to produce controlled anisotropy with discrete, anisometric elements in a 2D model. This technique offers a high-throughput system to study the effects of different physical parameters with defined dimensions and interelement distances on axonal growth and alignment, and thus, to obtain a deeper understanding of axon navigation in contact with biomaterials.[38] The substrate is coated with gelatin, and primary sensory nerve cells harvested from chick dorsal root ganglia (DRGs) are cultured. The ability of neurons and other cells to continue growing in a pre-defined direction after they lose their guidance cue is ventured into. Although in vitro surfaces have previously been employed to understand the influence of substrate geometry and topographies on axonal growth and neural tissue guidance,[20,30,39–41] the role of discreet anisometric cues with discreet multi-axial, interelement spacing, acting as geometrical constraints to induce axonal guidance, has not been studied before. Such a system can provide information on the minimal physical guidance cues that are required for directed nerve growth, replacing the conventional continuous implantable scaffolds with new injectable regenerative therapies.[11,42]

2. Results and Discussion

2.1. Substrate Preparation

Custom-designed anisometric microelement arrays are 3D printed by TPL using the Nanoscribe system. These substrates are developed to understand cell–substrate interactions while allowing for long-term cell culture. An acrylate-based resin is printed onto acryl–silanized glass coverslips to produce polymeric anisometric microelements with various inter-elemental spacings (**Figure 1**a). The computer-aided design enables rapid fabrication of multiple array micropatterns on a single glass substrate, which allows for testing one cell population on multiple differently spaced microelement patterns. The fabricated substrate is robust and transparent allowing bright field imaging for time-lapse microscopy, and the microelements show

**ADVANCED
SCIENCE NEWS**
www.advancedsciencenews.com
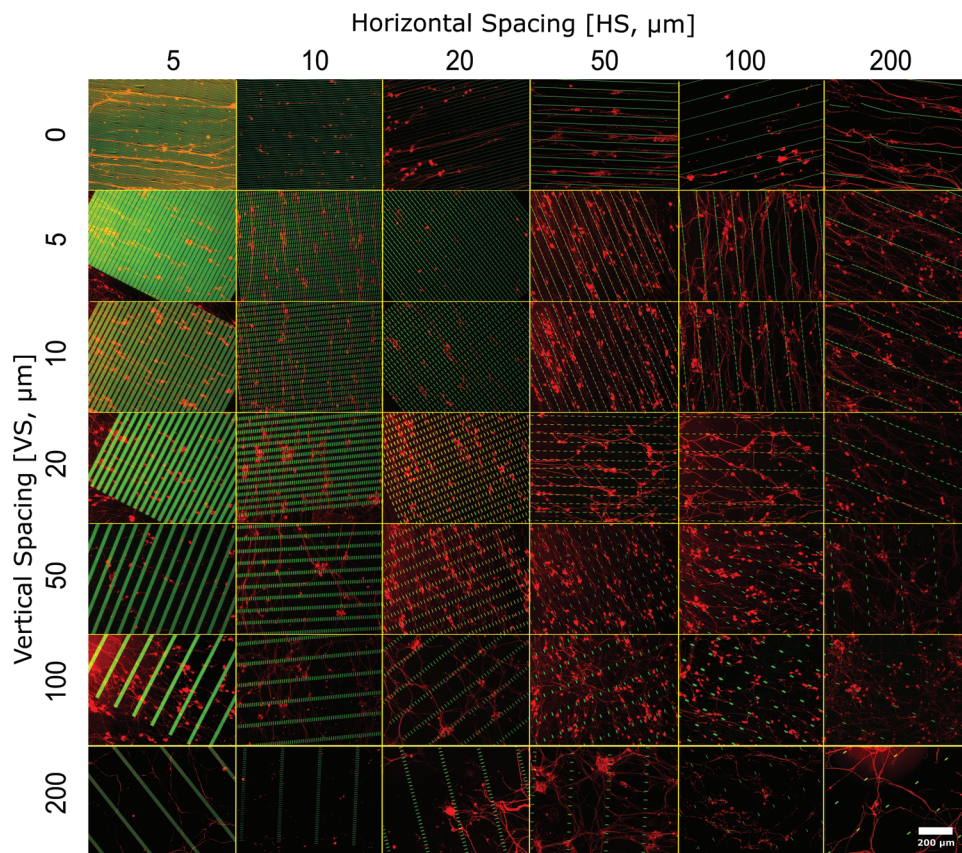
**ADVANCED
HEALTHCARE
MATERIALS**
www.advhealthmat.de

Figure 1. Development and fabrication of micropattern substrates. A) Schematic of two-photon lithography to develop microelements from computer-aided design. The micropattern is designed with custom inter-element spacing by varying the horizontal spacing (HS) and vertical spacing (VS) on a single substrate in high-throughput. B) Comparison of neurite coverage among different cell-adhesive coatings showing higher neurite outgrowth on gelatin and fibronectin coatings. C) Scanning electron microscopy (SEM) images of micropatterns show i–iii) highly ordered two-photon polymerized microelements that autofluorescence in the green channel. iv) Cells align along the microelements. The ability of cells to sense the microelements and stretch in between them is observed. v) Cell–material interaction (arrowheads) is achieved by the exploration of the vi) finger-like projection of filopodia and vii) web-like structures of lamellipodia. viii) Some cells are observed interacting with the microelement from the top reaching the bottom of the substrate. Arrowhead: lamellipodia, filopodia and cell–material interaction; double-headed arrow: microelement. Data presented as mean ± SD, $n \geq 3$, P values are calculated using one-way ANOVA with Bonferroni correction, $*P < 0.05$, $**P < 0.01$.

auto-fluorescence that can be detected at excitation: 480–550 nm (Figure 1c-ii). To improve cell–substrate interactions, the resulting high precision microstructures (Figure 1c-i,ii,iii) are coated with cell adhesive proteins and poly-L-lysine (PLL). Anisometric microelements with dimensions 20 × 1 × 10 µm (length × width × height, aspect ratio of 20) are used in this study. In order to provide a pseudo-3D environment,[20] the height of the microelements was set to 10 µm in an attempt to prevent neurites from crossing over them (Figure 1a). Micropatterns are fabricated with horizontal spacings (HS) ranging from 5 to 200 µm (distance between elements at their longest side), and vertical spacings (VS) between 0 and 200 µm (distance between elements at their shortest sides). Substrates without vertical spacing are continuous and act as a positive control while flat substrates without any micropatterns are used as a negative control. The space between the microelements creates a paradigm for the cells and axons to decide their growth direction. By varying the inter-element distance, it is possible to systematically study and understand its role in neurite alignment and the ability of the elements to promote unidirectional growth.

2.2. Cell–Substrate Interactions

Since the cells and neurites normally do not attach to unmodified glass or the acrylate-based microelements, various cell-adhesive

molecules were tested to be used as a coating to improve cell attachment. Poly-L-lysine was shown to support nerve growth through interactions of its positive electrostatic charge interaction with the negatively charged ions in the cell membrane and was compared to ECM proteins, such as fibronectin and laminin, and gelatin (derived from collagen) (Figure 1b).[43,44] Fibronectin, followed by gelatin and laminin, shows high neurite growth per covered area but 10 mg mL⁻¹ gelatin was selected for coating the substrates due to its lower costs. The resulting SEM images of highly ordered microelements (double-headed arrow) (Figure 1c-i) with cultured cells demonstrate cell–substrate interactions (arrowheads), where cells align in between and across multiple microelements (Figure 1c-iv) and stretch to connect the microelements (Figure 1c-v). This suggests that the gelatin coating is present on both the glass and polymerized microelements. At higher magnification, the cell structures resemble both cell lamellipodia and filopodia (white single-headed arrowheads) probing and adhering to the walls of the microelements (Figure 1c-vi, vii). Few cells are also observed on the top of the microelements and stretch to reach the bottom of the substrate (Figure 1c-viii). Their ability to sense the biochemical cues for anchorage allows the cells to gather information about the substrate and to find suitable paths to follow. The integrin-binding sites, present in the ECM molecules, provide a chemical stimulus to create contact attachment points, that alter the motility of the

**ADVANCED
SCIENCE NEWS**

www.advancedsciencenews.com

**ADVANCED
HEALTHCARE
MATERIALS**

www.advhealthmat.de

Figure 2. DRG cultured for 3 days and immunostained (TUJI) on micropatterns with different interelement spacing. An array of varying interelement spacing ranges from 0–200 μm in VS and 5–200 μm in HS. The microelements are observed in the green channel and the nerve cells are observed in the red channel.
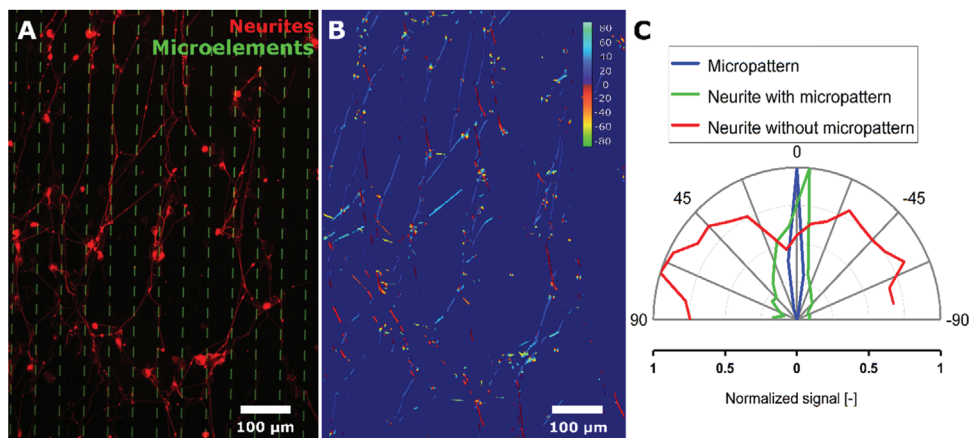
growth cone (GC) by activating specific integrin receptors in the cells, leading to subsequent secretion of ECM proteins resulting in modification of their environment.[45]

2.3. Influence of Inter-Elemental Spacing on Neurite Orientation

The micropattern arrays with patterns presenting 36 different combinations of inter-elemental distances (HS and VS) were studied and networks of polarized nerve cells extending their axons were observed on the bio-functionalized substrates with anisometric microelements (**Figure 2**; Figure S1, Supporting Information). The anisotropy created by the microelements influences the growth direction of the neurites (**Figure 3**a). Overall, we observe that the increase in inter-elemental distance (either VS or HS) above a certain threshold decreases neurite alignment along the microelements. Fluorescence micrographs show a combination of microelements (green) and β-tubulin stain (red) (Figure 3a). An elliptical orientation kernel is used to determine the direction of the neurites and is represented by a color-coded image (Figure 3b). By filtering out the bodies of the nerve cells, interference with the alignment analysis is prevented. The shape of the orientation distribution of the microelements distinguish between neurites grown on a flat substrate without a micropattern array, and the neurites in the presence of a micropattern

array (VS: 20 μm, HS: 50 μm) (Figure 3c). The presence of the aligned microelements influences neurite outgrowth along the major axis of the microelements as indicated by the narrow distribution (green line) close to that of the highly aligned microelements (blue line). In contrast, orientation of neurite growth in the samples without any micropattern has a broad distribution with multiple peaks (red line). Introduction of the anisotropic microelement array facilitates neurite guidance and results in oriented extension along the microelements, resulting in a narrow distribution with a peak around a preferred direction (indicated as 0°), depending on the inter-element spacing. These results are in accordance with the study performed on discreet microcones showing that neurite alignment is higher for anisometric microcones in comparison to isometric microcones.[35]

To study the degree of neurite orientation in between microarray patterns with different vertical and horizontal spacing, the discreet orientation distribution of neurites is normalized to the maximum count in the histograms. As previously reported, neurite orientation parallel to the channel wall of continuous microchannels was higher for channel widths of 20–30 μm, compared to wider channels (up to 60 μm) and to that of flat substrates.[46] In this report, this width is associated with the HS parameter. Therefore, to investigate the effect of discontinuous tracks, arrays of microelements (20 × 1 × 10 μm, Length × Width × Height) presenting VS between 0 and 200 μm under a constant

**ADVANCED
SCIENCE NEWS**
www.advancedsciencenews.com
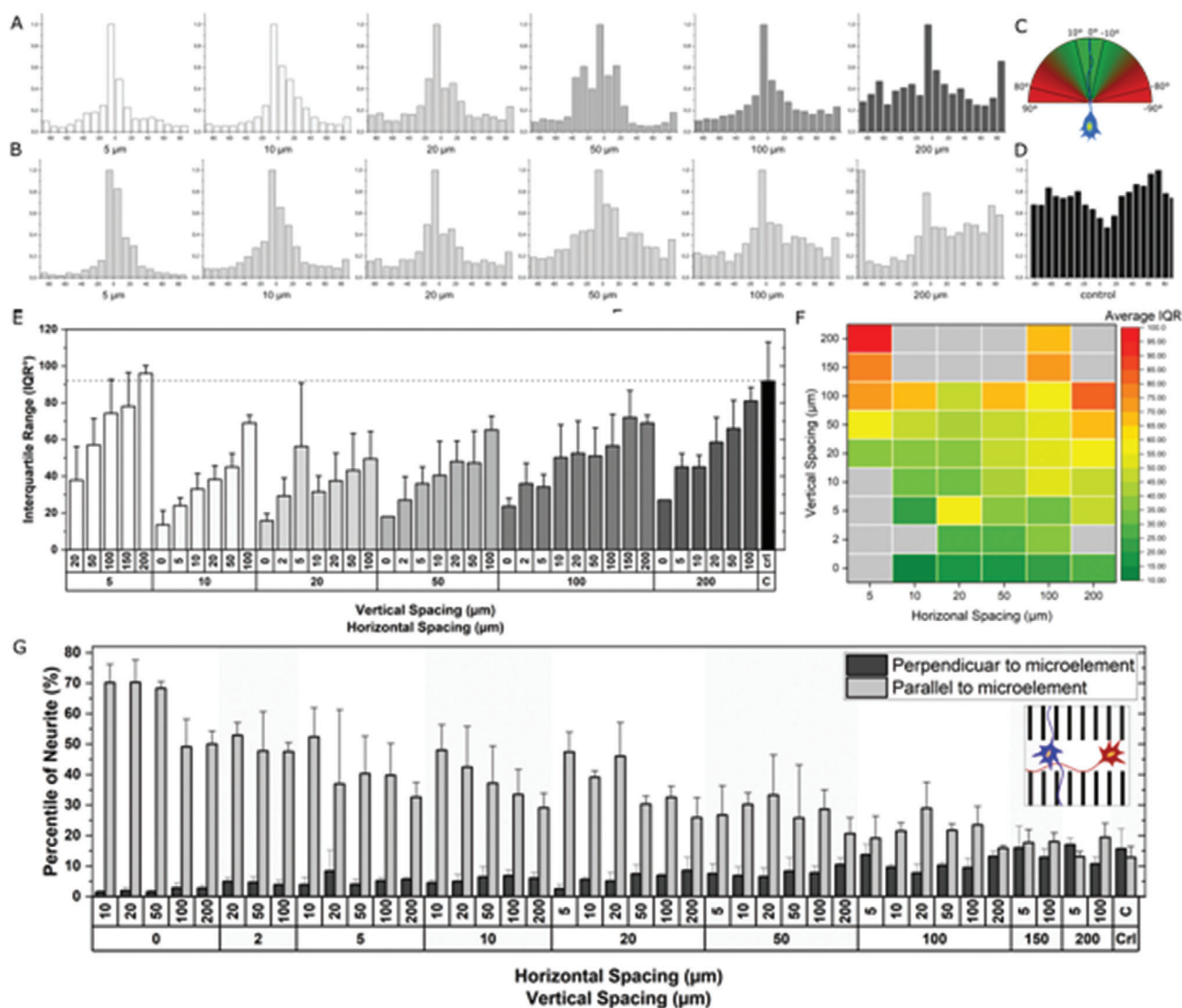
**ADVANCED
HEALTHCARE
MATERIALS**
www.advhealthmat.de

Figure 3. The images are processed to obtain the orientation distribution of the extending neurites on the micropatterned substrate. The multichannel image (A) is split into its corresponding channels revealing the primary orientation of the microelements. On applying the anisometric Gaussian orientation kernel, an alpha image (B) is generated to depict the direction of the neurites. C) The orientation distribution around the direction of the anisometric microelements (0^0) obtained is further plotted, here for VS: 20 µm and HS: 50 µm, to compare with the distribution of the microelements and the distribution of neurites without microelements (control). The shape of the distribution indicates the influence of the microelements on neurite alignment.

HS of 20 µm were used. As VS increases, the shape of the distribution changes from a sharp single peak distribution around 0° to a broadened and flattened distribution, an indication of loss of neurite alignment along the major axis of the microelements (**Figure** 4a,b). For a micropattern with a VS of 5 µm, the neurites are primarily guided along the major axis of the microelements. While, a peak at 90° can be observed in the case of a VS of 200 µm, suggesting that at long interruptions of the linear tracks, the short axis of the elements (1 µm wide) also provides physical guidance (Figure S2, Supporting Information). More importantly, even at this high VS up to 200 µm, the ability of the cells to recognize the anisometry of the microelements is evident as the shape of the distribution is still retained around 0° despite the peak observed at 90°. This demonstrates that the nerve cells respond stronger to the long axis of the guiding elements, even if vertically spaced at a distance tenfold higher than their length and HS. These observations illustrate the power aligned discrete microelements retain, compared to continuous guiding paths.

In contrast, when the VS is fixed at 20 µm and HS is varied (Figure 4b), the increase in HS influences the shape of the orientation distribution to a larger extent. At higher HS (200 µm), the orientation distribution gets shifted toward ±90° and the cells move along the guiding elements, as well as in between the guiding elements, resulting in the major fraction of neurites oriented in the direction perpendicular to the long axis of the microelements. Understanding the role of physical guidance along the major or minor axis of anisometric microelements is crucial in systems where changing the VS or HS or both, alters neurite growth direction. When primary neurons are cultured on a flat gelatin-coated substrate without microelements, their axonal extension is random without any directionality and thus, no principal peaks in the orientation distribution are observed (Figure 4d).

The neurite orientation distribution is measured ranging from −90° to 90° with the major axis of the microelements orienting at 0° (Figure 4c). This distribution is analyzed by determining the interquartile range (IQR) (Figure 4e,f). The IQR is calculated

as the difference between the angle (°) at the 75th percentile of neurite orientation and the 25th percentile of neurite orientation depicting the "middle 50%" of the neurite orientation distribution. This allows for the quantification of neurite orientation along a certain direction. Lower IQR values (<90°) indicate over 50% of the neurite orientation along a certain direction, whereas higher IQR (>90°) suggests random neurite outgrowth. While the IQR reveals oriented growth in a specific direction, it does not convey whether this direction is along the microelements. Hence, an additional parameter is needed to measure the neurite orientation along the major (parallel) and the minor axis of the microelements (perpendicular) (Figure 4g). The combined information provided by the IQR and the percentage of neurites parallel or perpendicular to the microelements reveals the neurite growth direction. It is intuitive to assume that at a lower inter-element spacing, neurite alignment increases, in contrast to higher inter-element spacing with less physical guidance cues. This is confirmed by the higher IQR values that are obtained when the VS increases for a fixed HS (Figure 4e,f). On the other hand, the orientation distribution histograms (Figure 4a,b) demonstrate that discreet microelements can provide physical guidance for the neurites to grow along the major axis of the microelement even at large VS up to 50–100 µm, depending on HS. Despite the continuous alternating probing of the growth cone, neurites tend to retain quasi linear paths due to their inherent rigidity and resistance toward bending.[47] This supports our observation that interrupted guidance cues are able to provide sufficient support to sustain unidirectional growth even with large spacing between them. In contrast, a different trend is observed for the IQR when HS increases at a constant VS. In this case, an initial decrease in IQR is observed when HS increases from 5 to 10 or 20 µm, which could be due to the lack of space for the neuronal cell bodies (≈10 µm) to reach and adhere to the bottom of the substrate when HS is too small. Even though the cells can deform to adjust to this topographical constraint, most of the cells were observed on top of the microelements with only

ADVANCED
SCIENCE NEWS
www.advancedsciencenews.com

ADVANCED
HEALTHCARE
MATERIALS
www.advhealthmat.de

Figure 4. Orientation analysis of immunostained DRG neurons cultured on micropatterns with different inter-elemental spacing VS and HS. A) Orientation distribution of neurites with a fixed HS (20 µm) and variable VS (5–200 µm). B) Orientation distribution of neurites with a fixed VS (20 µm) and variable HS (5–200 µm). C) A pictorial description of neurite orientation in a polar coordinate system. D) Negative control substrate without any microelements. E) The IQR of all the micropattern conditions with altering VS and HS. F) Map showing average IQR for different combinations of HS and VS. G) Percentile of neurites growing along the direction of the microelements, as well as perpendicular to the direction of the microelements. G-inset) Schematic representation of neurite growth along the major axis of the microelement (blue) and minor axis of the microelement (red). Data presented as mean ± SD, $n \geq 3$.

some axon protruding to reach the bottom of the substrate for a micropattern array with HS equal to 5 µm. These observations are in line with previously reported continuous microchannels (channel width of 5 µm, height of 25 µm), where reduced neurite outgrowth was observed.[48] As aligned neurites have a positive feedback effect on the directionality of neighboring neurons, fewer axons can negatively influence overall alignment and thus result in higher IQRs. Therefore, there is a critical lower limit for HS ≈ 10 µm to provide sufficient space for the neuronal bodies to settle in between the microelements leading to neurite polarization (Figure S3, Supporting Information). The IQR trend for HS > 10 µm shows an increase with increasing HS at

constant VS. In comparison, the previously reported study on neurite alignment in the presence of discreet periodic, isometric, micropillars (1 µm diameter, 5 µm height) showed an increase in neurite alignment when HS increased from 3 to 12 µm for a constant VS of 3 µm.[49] Here, neurons were also mainly growing on top of the topography in the case of HS and VS equal to 3 µm. Interestingly, for the several micropattern arrays tested here, neurite orientation remains oriented along the major axis of the microelement. Highly aligned neurite networks are observed at lower VS (5–50 µm), in combination with a range of HS (10–200 µm) showing little dependency of the IQR–VS trends to HS during physical guidance. For micropattern arrays with

VS $\geq$ 150 µm at HS of 5, 100, or 200 µm, IQR values above 90° were observed.

The ability of the neurites to retain their growth direction in between the microelements depends on the proximity of the guidance cues available. The neurites have two possible directional cues available after they lose their physical guidance (Figure 4g, inset), either perpendicular (red) or parallel (blue) to the microelement. An elliptical, "Mexican hat" orientation kernel is employed to measure the orientation of neurites and the percentages of neurite segments (N_s) growing along the major axis of the microelements (parallel, ($0° \pm 9°$)) or the minor axis of the microelements (perpendicular, ($-81° > N_s > 81°$)) are studied for different inter-elemental spacing HS and VS (Figure 4g, Experimental Section). The percentages of neurites growing in parallel and perpendicular to the microelements are consistent with the IQR data (Figure 4e,f), with the percentile of neurites growing in parallel to the major axis being the highest at low VS (2–20 µm) for all tested HS, while it reduces gradually with increasing VS. In contrast, the fraction of neurites growing perpendicular to the microelements is increasing with increasing VS. At higher HS (100, 200 µm), HS equal to 5 µm, and VS (100, 150, 200 µm), neurite growth shows limited directionality with similar low fractions of neurites ($\approx$15–20%) growing perpendicular or parallel to the microelements, demonstrating a behavior that mirrors that of flat control substrates. The maximum difference in parallel versus perpendicular neurite growth is observed at a VS of 5 µm and HS of 10 µm, where >52% of the neurites align along the microelements and only <4% orient perpendicular to the microelements. As nerve cells follow the major axis of the micropatterns, changing the micropattern orientation changes the primary growth direction (Figure S4, Supporting Information).

In view of developing scaffolds with minimal guiding cues, and therefore less material, estimating the space occupied by the guiding elements is of great importance. Our research shows that in comparison to the volumes occupied by a continuous guidance cue, the space occupancy of discrete guidance cues under similar conditions can be reduced by 20 vol% (Figure S5, Supporting Information). Arrays of microelement with different VS and HS but similar percentages of neurites growing parallel to the microelements also have comparable IQR values. As an example, a neurite orientation distribution of IQR $\approx$ 35°, $N_{s\parallel} \approx$ 45%, and $N_{s\perp} \approx$ 4% is observed in micropatterns with both large HS and small VS (HS: 100 µm, VS: 2 µm), as well as for equally spaced HS and VS (20 µm). In the first case, the pattern takes up 91% of the total guidance area that would be occupied by single continuous guides of the same width, while the equally spaced micropattern reduces the guidance area further to only 50%. However, when looking at the total volume occupied by the microelements in the array, the HS = 100, VS = 2 array takes only 0.90% of the total volume, compared to 2.38% occupied by the elements that are equally spaced (Figure S6, Supporting Information). In contrast, at high VS and low HS, (HS: 5 µm, VS: 200 µm), we observe that the percentile of neurites growing perpendicular to the microelements ($N_{K\perp}$ 16.99%) is higher than those growing in parallel ($N_{K\parallel}$ 13.03%) (Figure 4g). This shows that the directional guidance cue imparted by the long axis of the anisometric microelements can be overruled by spatial arrangements of the guidance cues with low HS and high VS.

In the case of an injectable Anisogel, in which anisometric, magneto-responsive guiding elements align in situ, it is challenging to obtain anisometry in interelemental spacing. Hence, a more isometric HS and VS has been achieved in our previous reports, showing that a distance of $\approx$22.5 µm is the most efficient inter-microgel spacing for nerve guidance in 3D fibrin-based Anisogels using rectangular microgels (width 2.5 µm, length 50 µm) with aspect ratio of 20. Here we demonstrated that thinner elements (2.5 µm versus 5 µm width) enhance the rate of nerve growth due to a reduced cross section, which can impair neurite extension in the direction parallel to the long axis of the elements.[50] As an axon has a diameter of 1 µm, we choose this as width for our elements and an aspect ratio of 20.

2.4. Supporting Cells Influence Axonal Directionality

The orientation of the neurites is influenced by the microelements but can also be affected by the other supporting cells and their alignment. This can be observed by performing live imaging of the cultures on the micropattern platforms (**Figure 5**a,b). Bright field time-lapse analysis shows the growth cones of the nerve cells exploring their surroundings. The GC acts as a motile growth sensor and is affected by physical[51] and chemical[52] factors, which result in signaling cascades causing morphological and directional changes.[53,54] During the advancement of the GC, an alternate exchange between stochastic and deterministic behavior occurs, with a transition step in between, where the cues of the environment influence the steering of the neurite axon.[55] Unlike previously reported observations,[48] where cells are spatially restricted along continuous ridges of the groove, the GC in our setup senses its local environment in all directions, detecting the periodic guidance from the microelements and steering in between the microelements (Figure 5a). It was observed that GC exploration and directionality are influenced by the neighboring cells, as the GC can form temporary or permanent connections with these cells. In some cases, the GC chooses the shortest path to connect to its neighboring cells ignoring the influence of the microelements when it has the choice to follow a microelement or to connect with another neuron or supporting cell in its direct vicinity. This is likely due to chemoattractants produced by the cells. As the influence of the supporting cells is sometimes stronger than the influence of the micropattern, axons can grow perpendicular to the major axis of the microelements to form a neural network (Figure 5b). Neurons have the innate ability to make connections to other neurons and in some cases to other types of cells, such as epithelial tissues, for cell–cell communication. They undergo morphogenesis to grow and extend as neurites until the neurons form a circuit connecting the brain and body.[56,57]

In the case of a microelement array with VS = 20 µm and HS = 50 µm (Figure 5c), an IQR of $\approx$50° is observed, where $\approx$30% of neurites grow along the major axis of the microelements, and $\approx$7.5% grow along the minor axis of the microelements. In this case, although a major component of neurite growth is along the microelements, the proximity of the other cells has a strong influence on the direction of the neurite alignment. Unfortunately, it is very difficult to decouple the influence of proximal cells and microelements on neurite alignment as the supporting/other cells
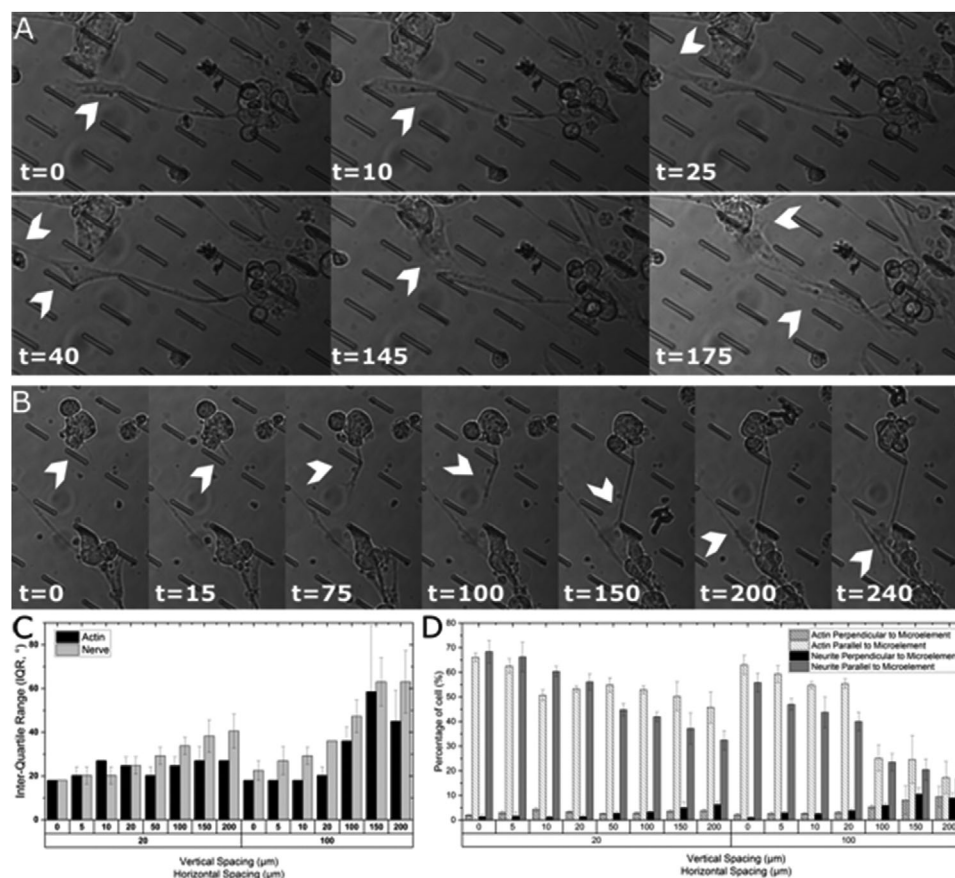
Figure 5. Influence of microelements and supporting cells on the neurite steering direction. i) Live imaging of axonal steering on anisometric micropattern substrates. Different time points (minutes) reveal that the axons steer in between the microelements, sensing different physical cues and other cell bodies. Micropatterns with interelemental spacings of VS = HS = 20 µm and ii) VS = 20 and HS = 50. (Scale: Length of microelement = 20 µm). iii) IQR corresponding to the orientation of neurites and actin positive cells. iv) Percentile of cell growth along the major and minor axis of the microelements for neurites and actin positive cells. Data presented as mean ± SD, $n \geq 3$.

are an integral part of any neural network and their morphology is also affected by the microelement patterns. Comparing the GC motility between a micropattern array and flat control substrates reveals that the guiding microelements play a major role in the realization of directed neural networks. The supporting cells stained for actin filaments are oriented along the direction of microelements for inter-elemental spacing smaller than the cellular dimensions (Figure S7, Supporting Information). This is consistent with previously reported work, demonstrating actin and nuclear reorganization of cells in confined spaces.[58] The orientation distributions (IQR) of the actin positive cells and neurites are compared with each other for VS 0–200 µm at a HS of 20 or 100 µm (Figure 5c; Figure S7, Supporting Information). For each stain individual, an increase in IQR is observed for increasing VS, with a steeper increase in the case of HS: 100 µm. This denotes a stronger influence of VS along the major axis of the microelements for a large horizontal spacing. Comparing the percentiles of cells oriented perpendicular and parallel to the microelements, a similar trend is observed (Figure 5d). With decreasing VS for a given HS, the fraction of neurites and supporting cells, oriented parallel to the microelements, increases. Therefore, the results demonstrate that the orientation of sup-

porting cells is also influenced by the inter-elemental spaces between the microelements and may thus indirectly affect neurite directionality.

3. Conclusion

A microelement array with custom-designed, anisotropic, and discreet guiding cues was developed to study the ability of discontinuous elements to influence the orientation of neurite outgrowth in a systematic, high-throughput manner. A methodic alteration in both the vertical and horizontal inter-element spacing between the microelements reveals their interplay in inducing neurite alignment for the first time. As expected, an increase in neurite alignment occurs along the major axis of the microelements at lower horizontal and vertical distances. A microelement array with a VS of 5 µm and a HS of 10 µm showed the highest neurite alignment (>52%) parallel to the major axis of the microelement, with only <4% neurite extension perpendicular to this direction and an IQR of ≈24°. This array is associated with a reduction in the total volume of guidance cues by 20% in comparison to continuous patterns. Interestingly, micropatterns resulting in similar neurite alignment (IQR ≈ 36°) are

observed with different HS and VS combinations, leading to different total volumes needed as guiding elements. This shows that the amount of material required as guiding cues can be reduced without compromising cell guidance, proving that it is possible to develop highly efficient orientation systems. In addition, moderate alignment (IQR < 50°) is observed at smaller VS (5 µm) with larger HS (200 µm) and for larger VS (100 µm) and with smaller HS (20 µm). Overall, this report shows the power of discrete anisotropic guiding elements to orient neurite outgrowth, while the minimal amount of physical guidance can be determined by altering the inter-element spaces. While we demonstrate that several micropattern arrays with anisometric interelemental distances showed directed neurite growth in a 2.5D system, achieving a similar approach in a full 3D system presents a challenge due to limitations in generating arrangements with defined asymmetric HS and VS. Furthermore, live time-lapse imaging of these in vitro platforms revealed that neighboring cells (neurons or actin positive supportive cells) in combination with anisometric microelements play a role in creating a directed neural network. The results of this work bring us one-step closer to understanding the complexity of the formation of neural tissue by physical microfeatures. This information can be used for the development of engineered tissue regeneration strategies such as 3D injectable scaffolds that aim to provide minimal guiding cues for directed nerve growth and repair.

4. Experimental Section

Microfabrication of Microelements: The design of the base microelement with dimensions of length 20 µm, width 1 µm, and height 10 µm and the patterns with different interelement spacing ranging from 5–200 µm in horizontal spacing and 2–200 µm in vertical spacing were designed in G-code using software DeScribe 2.5.3 (Nanoscribe GmbH). All the micropatterns in this study were fabricated using TPL (780 nm, ≈100 fs, 80 MHz), using a 63× NA, 1.4 immersion-based objective with a voxel size of $xy = 0.25$ µm and $z = 0.4$ µm enabling the fabrication of structures at a resolution <1 µm. The patterns were printed on acryl–silanized glass coverslips to improve attachment of the elements to the substrate.

Surface Functionalization: Ø30 mm glass coverslip (Menzel Glaser # 1.5, Thermo Scientific, USA) was cleaned with isopropanol/acetone (Sigma–Aldrich, ≥99.8%) in an ultra-sonication bath for 5 min. The cleaned glass coverslips were incubated in a 0.8% v/v solution of 3-(trimethoxysilyl) propyl acrylate (Sigma–Aldrich, 92% with 100 ppm butylated hydroxytoluene) in acetone overnight at room temperature. This allowed the crosslinking between the photoresist and glass substrate at its interface improving microelement anchorage on the substrate. The silanized glass substrates were rinsed with deionized water and dried in a flow of nitrogen.

TPL: 100 µL of photoresist (IP-L 780) was drop cast on the silanized substrate. Laser power 60%, scan speed 20 000 µm s⁻¹, and galvo mirror speed 300 µm s⁻¹ was optimized. The smallest photo polymerization volume (1 voxel) had an elliptical shape with a width of 0.33 µm and a height of 0.80 µm. These were printed layer-by-layer with a slicing distance of 0.5 µm. The uncrosslinked polymer resin was dissolved using propylene glycol monomethyl ether acetate (PGMEA), (Sigma–Aldrich, ≥99.5%) for 30 min at room temperature and washed with isopropanol. The substrate was dried in a flow of nitrogen.

Bio-Functionalization: Substrates were individually coated using different biomolecules such as poly-L-lysine (0.1 mg mL⁻¹, PLL, Sigma–Aldrich); mouse laminin (10 µg mL⁻¹, Invitrogen); PLL (0.1 mg mL⁻¹); and laminin (10 µg mL⁻¹, PLL-Laminin) in combination; human fibronectin (10 µg mL⁻¹, Sigma–Aldrich); gelatin (10 mg mL⁻¹, Sigma–Aldrich, from bovine skin) at 37 °C for 30 min and dried at room temperature.

Cell Culture: Dissociated dorsal root ganglions (DRG) extracted from 10-day old chicken embryos were dissected and cleared from other supporting tissues and temporarily collected in Hank's balanced salt solution (HBSS) supplemented with 6 g L⁻¹ glucose. Pooled DRGs were then dissociated into single primary nerve cells (PNCs) by incubating them in Trypsin (1X, Sigma–Aldrich) for 30 min at 37 °C, followed by trituration through a fire-polished glass pipet several times until a single cell suspension was obtained. The cells were panned for 2 h at 37 °C to obtain pure neuronal cells by separating adherent cells such as fibroblasts and Schwann cells. The cells were suspended in Dulbecco's modified eagle medium (DMEM), supplemented with 10% fetal bovine serum (FBS), 1% antibiotics/antimycotics (AMB), and 20 ng mL⁻¹ of β-nerve growth factor (NGF, Peprotech). The seeding density of the cells was controlled by using PDMS rings to confine the area of cell growth on the micropattern. A seeding density of 150 cells mm⁻² was chosen to study the growth of neurites and cultured at 37 °C, 5% CO₂, and 95% humidity for 3 days. DRG tissue was extracted in accordance with the local animal ethics regulations and the European Directive 2010/63/EU.

Immunostaining: After 72 h in culture, PNCs were fixed in prewarmed (37 °C) 4% paraformaldehyde (PFA, AppliChem) in phosphate buffer saline (PBS, 1×, pH 7.4) for 20 min. The substrate was washed twice with PBS and permeabilized using 0.1% Triton X-100 (Sigma–Aldrich) in PBS for 3 min. After a short PBS wash (2×), substrates were incubated with primary anti-tubulin (1: 250, TUJ1 monoclonal antibody mouse-derived, Biolegend) in 5% bovine serum albumin (BSA, Sigma–Aldrich) in PBS solution for 4h at RT, and washed twice for 30 min with PBS. The secondary antibody Alexa Fluor 633 goat anti-mouse was added and incubated for 2 h followed by a final PBS wash. To stain actin, phalloidin-iFluor 594 (1: 1000, Abcam) was added, and incubated for 2 h. Samples were counterstained using 4′,6-diamidino-2-phenylindole (DAPI) (1: 100, Thermo Fischer Scientific) by incubating the substrate for 10 min followed by PBS wash (2×) for 30 min.

Imaging: Samples were visualized with a Zeiss Axio Observer Z1 microscope equipped with an Axiocam MRm camera or with a laser scanning confocal microscope (SP8 Tandem Confocal, Leica Microsystems Inc.). In the case of SP8, the light sources were a diode 405 (for DAPI fluorescence), argon-ion laser adjusted to 488 nm emission (fluorescence from microelements), diode-pumped solid-state laser 561 nm (iFluor 594), and helium-neon laser 633 nm (Alexa Fluor 633). The images were acquired in sequential channels or with suitable detector settings to avoid cross-talk between signals. The substrates were imaged with 20 µm Z stack height with a slicing distance of 1 µm. Image processing was performed using LasX, AxioVision, Image J, and Python.

Neurite Orientation Analysis: Neurite alignment induced by the microelements was quantified by analyzing the beta-tubulin signal (red channel) and the microelements signal (green channel). A slight overlap of the microelement signal was still observed in the neurite images, which was then eliminated by subtracting the microelements from the neurite resulting in a signal corresponding only to tubulin. The orientation of the tubulin positive structures was analyzed using an elliptic differential kernel. The kernel was calculated as a rotated "Mexican hat" (the second derivative of a 2D Gaussian) function with a broad and narrow width in X and Y direction, respectively. The procedure had the following main steps. (i) Background correction and highlighting features. (ii) Constructing binary masks. (iii) Convolution with the rotated kernel. (iv) Identifying orientation based on the highest intensity in the convolved images along the angle axis (Z-axis), then removing unwanted data points applying the binary masks defined above in (ii).

Background Correction: Images were blurred using a Gaussian kernel with a radius of 60 pixels (matrix size: 121 × 121 pixels) and standard deviation (σ) of 20 pixels. This background was subtracted from the image, and negative values were set to zero. The image was then smoothed using another Gaussian kernel, with a window radius of 5 pixels (matrix size 11 × 11 pixels), and width (σ) of 1 pixel. The dynamic range of the image was then compressed around its mean value applying a square root function. In detail, first the image was divided by its mean value, then the square-root was applied, and the result was multiplied back with the mean.

Binary Masks: Two types of binary masks were created. One was using the image of the microelements. This image was converted to a binary image keeping all pixels below 50% of its maximal intensity. The pattern was further eroded using a simple erosion operator two times. This removed every pixel which had at least one zero neighbor. Data were kept where this filter was nonzero. The second filter used a structure tensor to characterize the local neighborhood of each point. Blobs were assumed for relative intensities above 1% of the amplitude maximum, where the coherence around each point was less than 0.5.[59,60] The local neighborhood was 5 times the size of the smoothing filter. Data were removed where this filter was nonzero.

Convolution with Kernel and Maximum Image: Convolution with the rotating kernel resulted in a set of 2D images, forming a Z-stack, where the Z-axis was the orientation angle of the kernel. The maximum was collected along this Z-axis for each pixel into a "maximum image", and the angle where this maximum occurred was recorded into an "alpha" image. A threshold was applied to this maximum image using Otsu's method, and all points were erased below this threshold. Then, those points were also removed which were defined by the binary masks above. The remaining points were used to collect the corresponding angular values (discreet intervals of 9° between −90° and +90°). A histogram was determined from the angles. The whole process was implemented in Python, and the core functions are available online as part of the ImageP package on Launchpad [https://launchpad.net/imagep]. Alternatively, the angular values are post-processed in R and the angles are reoriented to the angle defined by the microelements in order to compare the relative orientation properties.

Statistical Analysis: Data points are shown as mean average with error bars indicating standard deviation with sample size ≥ 3. One-way ANOVA and pair comparisons using Bonferroni and Tukey's methods were performed to determine statistical significance, and the p values for statistical significance are represented with stars: $*p < 0.05$, $**p < 0.01$. Statistical analysis was done using OriginPro 2020.

Supporting Information

Supporting Information is available from the Wiley Online Library or from the author.

Conflict of Interest

The authors declare no conflict of interest.

Data Availability Statement

Research data are not shared.

Keywords

[1] L. De Laporte, Y. Yang, M. L. Zelivyanskaya, B. J. Cummings, A. J. Anderson, L. D. Shea, *Mol. Ther.* **2009**, *17*, 318.

[2] C. D. L. Johnson, D. Ganguly, J. M. Zuidema, T. J. Cardinal, A. M. Ziemba, K. R. Kearns, S. M. McCarthy, D. M. Thompson, G. Ramanath, D. A. Borca-Tasciuc, S. Dutz, R. J. Gilbert, *ACS Appl. Mater. Interfaces* **2019**, *11*, 356.

[3] K. Pawar, B. J. Cummings, A. Thomas, L. D. Shea, A. Levine, S. Pfaff, A. J. Anderson, *Biomaterials* **2015**, *65*, 1.

[4] Y. C. Chang, M. H. Chen, S. Y. Liao, H. C. Wu, C. H. Kuan, J. S. Sun, T. W. Wang, *ACS Appl. Mater. Interfaces* **2017**, *9*, 37623.

[5] D. Hodde, J. Gerardo-Nava, V. Wöhlk, S. Weinandy, S. Jockenhövel, A. Kriebel, H. Altinova, H. W. M. Steinbusch, M. Möller, J. Weis, J. Mey, G. A. Brook, *Eur. J. Neurosci.* **2016**, *43*, 376.

[6] W. Ji, S. Hu, J. Zhou, G. Wang, K. Wang, Y. Zhang, *Exp. Ther. Med.* **2014**, *7*, 523.

[7] L. S. Wang, J. E. Chung, P. Pui-Yik Chan, M. Kurisawa, *Biomaterials* **2010**, *31*, 1148.

[8] E. Spedden, M. R. Wiens, M. C. Demirel, C. Staii, *PLoS One* **2014**, *9*, e106709.

[9] H. M. Geller, J. W. Fawcett, *Exp. Neurol.* **2002**, *174*, 125.

[10] M. Antman-passig, O. Sheffi, *Nano Lett.* **2016**, *16*, 2567.

[11] J. C. Rose, M. Cámara-Torres, K. Rahimi, J. Köhler, M. Möller, L. De Laporte, *Nano Lett.* **2017**, *17*, 3782.

[12] J. S. Chua, C. P. Chng, A. A. K. Moe, J. Y. Tann, E. L. K. Goh, K. H. Chiam, E. K. F. Yim, *Biomaterials* **2014**, *35*, 7750.

[13] K. J. Jang, M. S. Kim, D. Feltrin, N. L. Jeon, K. Y. Suh, O. Pertz, *PLoS One* **2010**, *5*, e15966.

[14] Y. A. Huang, C. T. Ho, Y. H. Lin, C. J. Lee, S. M. Ho, M. C. Li, E. Hwang, *Macromol. Biosci.* **2018**, *18*, 1800335.

[15] I. Tonazzini, E. Jacchetti, S. Meucci, F. Beltram, M. Cecchini, *Adv. Healthcare Mater.* **2015**, *4*, 1849.

[16] G. Piret, M. T. Perez, C. N. Prinz, *ACS Appl. Mater. Interfaces* **2015**, *7*, 18944.

[17] L. Wang, Y. Wu, T. Hu, P. X. Ma, B. Guo, *Acta Biomater.* **2019**, *96*, 175.

[18] A. Omidinia-Anarkoli, J. W. Ephraim, R. Rimal, L. De Laporte, *Acta Biomater.* **2020**, *113*, 350.

[19] H. Amin, M. Dipalo, F. De Angelis, L. Berdondini, *ACS Appl. Mater. Interfaces* **2018**, *10*, 15207.

[20] C. Leclech, M. Renner, C. Villard, C. Métin, *Biomaterials* **2019**, *214*, 119194.

[21] L. Micholt, A. Gärtner, D. Prodanov, D. Braeken, C. G. Dotti, C. Bartic, *PLoS One* **2013**, *8*, e66170.

[22] T. Repic, K. Madirazza, E. Bektur, D. Sapunar, *Sci. Rep.* **2016**, *6*, 39560.

[23] A. Omidinia-anarkoli, R. Rimal, Y. Chandorkar, D. B. Gehlen, L. De Laporte, J. C. Rose, K. Rahimi, *ACS Appl. Mater. Interfaces* **2019**, *11*, 7671.

[24] B. W. Tuft, S. Li, L. Xu, J. C. Clarke, S. P. White, B. A. Guymon, K. X. Perez, M. R. Hansen, C. A. Guymon, *Biomaterials* **2013**, *34*, 42.

[25] A. M. Almonacid Suarez, Q. Zhou, P. van Rijn, M. C. Harmsen, *J. Tissue Eng. Regen. Med.* **2019**, *13*, 2234.

**ADVANCED
SCIENCE NEWS**

www.advancedsciencenews.com

**ADVANCED
HEALTHCARE
MATERIALS**

www.advhealthmat.de

[26] C. Simitzi, A. Ranella, E. Stratakis, *Acta Biomater.* **2017**, *51*, 21.

[27] K. T. M. Tran, T. D. Nguyen, *J. Sci. Adv. Mater. Devices* **2017**, *2*, 1.

[28] J. A. Richardson, C. W. Rementer, J. M. Bruder, D. Hoffman-Kim, *J. Neural Eng.* **2011**, *8*, 046015.

[29] L. Xu, A. E. Seline, B. Leigh, M. Ramirez, C. A. Guymon, M. R. Hansen, *Otol. Neurotol.* **2018**, *39*, 119.

[30] F. Johansson, P. Carlberg, N. Danielsen, L. Montelius, M. Kanje, *Biomaterials* **2006**, *27*, 1251.

[31] G. R. Liguori, Q. Zhou, T. T. A. Liguori, G. G. Barros, P. T. Kühn, L. F. P. Moreira, P. Van Rijn, M. C. Harmsen, *Stem Cells Int.* **2019**, *2019*, 5387850.

[32] L. Yang, K. M. Jurczak, L. Ge, P. van Rijn, *Adv. Healthcare Mater.* **2020**, *9*, 2000117.

[33] A. Kundu, L. Micholt, S. Friedrich, D. R. Rand, C. Bartic, D. Braeken, A. Levchenko, *Lab Chip* **2013**, *13*, 3070.

[34] W. Li, Q. Y. Tang, A. D. Jadhav, A. Narang, W. X. Qian, P. Shi, S. W. Pang, *Sci. Rep.* **2015**, *5*, 1.

[35] C. Simitzi, P. Efstathopoulos, A. Kourgiantaki, A. Ranella, I. Charalampopoulos, C. Fotakis, I. Athanassakis, E. Stratakis, A. Gravanis, *Biomaterials* **2015**, *67*, 115.

[36] K. Baranes, N. Chejanovsky, N. Alon, A. Sharoni, O. Shefi, *Biotechnol. Bioeng.* **2012**, *109*, 1791.

[37] K. Baranes, D. Kollmar, N. Chejanovsky, A. Sharoni, O. Shefi, *J. Mol. Histol.* **2012**, *43*, 437.

[38] E. T. Stoeckli, *Development* **2018**, *145*, dev151415.

[39] M. Marcus, K. Baranes, M. Park, I. S. Choi, K. Kang, O. Shefi, *Adv. Healthcare Mater.* **2017**, *6*, 1700267.

[40] M. Cecchini, A. Ferrari, S. Micera, R. Stabile, A. Dhawan, I. Tonazzini, D. Pisignano, F. Beltram, *Nano Lett.* **2011**, *11*, 505.

[41] K. Wang, A. Bruce, R. Mezan, A. Kadiyala, L. Wang, J. Dawson, Y. Rojanasakul, Y. Yang, *ACS Appl. Mater. Interfaces* **2016**, *8*, 5082.

[42] A. Omidinia-Anarkoli, S. Boesveld, U. Tuvshindorj, J. C. Rose, T. Haraszti, L. De Laporte, *Small* **2017**, *13*, 1702207.

[43] A. Orlowska, P. T. Perera, M. A. Al Kobaisi, A. Dias, H. K. D. Nguyen, S. Ghanaati, V. Baulin, R. J. Crawford, E. P. Ivanova, *Materials* **2017**, *11*, 60.

[44] G. Ciardelli, V. Chiono, *Macromol. Biosci.* **2006**, *6*, 13.

[45] P. C. Kerstein, R. H. Nichol IV, T. M. Gomez, *Front. Cell. Neurosci.* **2015**, *9*, 244.

[46] M. J. Mahoney, R. R. Chen, J. Tan, W. M. Saltzman, *Biomaterials* **2005**, *26*, 771.

[47] M. J. Katz, *J. Neurosci.* **1985**, *5*, 589.

[48] A. Béduer, C. Vieu, F. Arnauduc, J. C. Sol, I. Loubinoux, L. Vaysse, *Biomaterials* **2012**, *33*, 504.

[49] M. Park, E. Oh, J. Seo, M. H. Kim, H. Cho, J. Y. Choi, H. Lee, I. S. Choi, *Small* **2016**, *12*, 1148.

[50] J. C. Rose, D. B. Gehlen, A. Omidinia-Anarkoli, M. Fölster, T. Haraszti, E. E. Jaekel, L. De Laporte, *Adv. Healthcare Mater.* **2020**, *9*, 2000886.

[51] D. E. Koser, A. J. Thompson, S. K. Foster, A. Dwivedy, E. K. Pillai, G. K. Sheridan, H. Svoboda, M. Viana, L. D. F. Costa, J. Guck, C. E. Holt, K. Franze, *Nat. Neurosci.* **2016**, *19*, 1592.

[52] S. M. Kim, M. Ueki, X. Ren, J. Akimoto, Y. Sakai, Y. Ito, *Int. J. Nanomed.* **2019**, *14*, 7683.

[53] D. Hoffman-kim, J. A. Mitchel, R. V. Bellamkonda, *Annu. Rev. Biomed. Eng.* **2010**, *12*, 203.

[54] L. A. Lowery, D. Van Vactor, *Nat. Rev. Mol. Cell Biol.* **2009**, *10*, 332.

[55] S. M. Maskery, H. M. Buettner, T. Shinbrot, *BMC Neurosci.* **2004**, *5*, 22.

[56] K. C. Flynn, *Bioarchitecture* **2013**, *3*, 86.

[57] K. E. Miller, D. M. Suter, *Front. Cell. Neurosci.* **2018**, *12*, 447.

[58] C. M. Denais, R. M. Gilbert, P. Isermann, A. L. McGregor, M. Te Lindert, B. Weigelin, P. M. Davidson, P. Friedl, K. Wolf, J. Lammerding, *Science* **2016**, *352*, 353.

[59] B. Jähne, *Digital Image Processing*, Springer, Berlin **2002**.

[60] M. Durande, S. Tlili, T. Homan, B. Guirao, F. Graner, H. Delanoë-Ayari, *Phys. Rev. E* **2019**, *99*, 62401.